Large-eddy simulations of dense-gas dispersion within a high-Reynolds number turbulent boundary layer

E. M. M. Wingstedt,[1,2,a)] M. Vartdal,[1] and B. A. Pettersson Reif[3]

[1] *Norwegian Defence Research Establishment (FFI), Kjeller, Norway*

[2] *University of Oslo, Department of Mathematics, Oslo, Norway.*

[3] *University of Oslo, Department of Technology Systems, Kjeller, Norway.*

(Dated: 17 July 2017)

Large-eddy simulations of flow over a backward-facing step with release of four different gases with increasing densities have been performed. The results have been analysed with particular emphasis on the part of the flow field sufficiently far downstream where the local effect of the source dynamics is no longer dominating the flow field.

The dense gas plumes maintain high concentrations close to the ground and become approximately twice as shallow in comparison to a neutrally buoyant plume. The vertical mixing is significantly reduced close to the ground and both momentum and scalar flux reversal are found in the two densest cases, indicating negative shear and buoyancy production of turbulence kinetic energy.

Examination of the gradient Richardson number indicates that all dense gases are significantly affected by buoyancy. Interestingly, a narrow layer within the plumes are identified where the impact of stratification are expected to be reduced. It is found that relaminarization is most likely occurring and that fluctuations found might originate from interfacial wave modes rather than from turbulence.

The large-scale structures are seen to resemble those found in plane channel flow close to the wall and further away from it. In the middle layer, significant differenced are found due to buoyancy effects. The large-scale structures become more pancake-shaped and with large-scale vorticity almost exclusively about the spanwise direction in the dense gas cases.

Keywords: LES; dense gas dispersion; backward-facing step; turbulence structures

[a] Author to whom correspondence should be addressed; Electronic mail: Emma-My-Maria.Wingstedt@ffi.no.

I. INTRODUCTION

Toxic industrial chemicals (TICs) are used in most countries and are produced, transported and stored in relatively large quantities. The potential consequences of accidental or intentional release of such compounds are of concern to the authorities. The wind field in urban areas are significantly affected by amongst others temporally unsteady separations and large recirculation regions downstream building structures. Release and transport of contaminants in urban environments are associated with complex physical and chemical processes. A particularly important characteristic of common TICs is that these are buoyant, i.e. heavier-than-air gases such as chlorine and sulphur dioxide, or lighter-than-air gases, such as ammonia. The buoyant nature of the contaminant can significantly affect the dispersion process. Under appropriate conditions, a lighter-than-air emission may rise from the ground whilst a heavier-than-air emission may remain near the surface, creating strong stable conditions that greatly reduce air entrainment and thus also the mixing process. Mixing can be effectively eliminated in regions of the urban terrain with very low wind speeds, such as recirculation zones downstream buildings, or in the vicinity of rapid terrain variations.

There exists a variety of different models and methods to predict the dispersion of contaminants. In recent years, computational fluid dynamics (CFD) has become a popular tool for this purpose. Several studies involving numerical simulation of dense-gas dispersion using the unsteady Reynolds-averaged Navier-Stokes (URANS) approach have been carried out with fairly good results[1–4]. This method is based on the assumption that the mean flow field is statistically unsteady, which is rather well suited for flows involving bluff body shedding occurring downstream of building structures. Perhaps an even more commonly used CFD approach is the simpler statistically steady RANS method[5–8]. Results often show that the mixing of scalar fields is underpredicted when using RANS, which may be explained by the method's exclusion of the inherent unsteady large-scale shedding.

The most physically appealing modelling approach that naturally includes the large-scale flow unsteadiness is large-eddy simulation (LES). LES resolves the inherent unsteadiness of the three-dimensional large-scale turbulence irrespectively of the nature of the averaged flow field, in addition to any feature associated with statistically unsteady shedding. Previous studies using the LES approach for urban dispersion modelling of neutral gases have shown good results in predicting flow and concentration fields[9–12]. However, the literature regarding

LES for dense-gas dispersion in complex geometries is scarce.

In this study, LES is utilized to study a neutrally buoyant, favourable pressure-gradient, turbulent boundary layer passing over a backward-facing step. A source from which neutral and dense gases are continuously released in the vertical direction is located immediately downstream the step. The main purpose of the study is to computationally investigate the effect of the released gas density on the dispersion process resulting from the interaction of the source with a separated turbulent flow field. Of particular interest is the effect on the dispersion far downstream of the source where the characteristics of the source no longer dictate the dynamics directly. This region is of interest because any kinematically relevant source characteristics that persist over large distances must be accounted for in dispersion models that operate on such scales. The back-step geometry is well suited for this purpose as it creates a recirculation region in its immediate vicinity as well as eliminates the upstream dispersion of the dense gas which in turn minimizes the region of interest. Also of interest is the effect of density differences on the turbulence structures.

II. PROBLEM FORMULATION

The domain of interest comprises an uphill slope followed by a backward-facing step of height h. A line source with $\Delta x = 1.5h$ is located just behind the back-step. The domain size is $(L_x/h, L_y/h, L_z/h) = (50, 28.8, 15)$ in the streamwise, spanwise, and wall-normal directions, respectively. The primary motivation of the backward-facing step is to limit the upstream effects of the source which is particularly emphasized in dense gas release[13,14]. The choice of an uphill slope was made in order to replicate the geometry from a set of wind-tunnel experiments where more complex dense-gas dispersion scenarios have been conducted[15]. The simulation of these experiments is a topic for future work. The moderate vertical momentum source significantly suppress the characteristic recirculation region downstream the back-step which enables a systematic comparison of the downstream development of different scalar fields with significantly different upstream behaviour. Figure 1 depicts the computational domain in the vicinity of the source. The inlet boundary is located at $x/h = -13.85$.

The incoming boundary layer thickness is approximately $H = 1$ m and the free-stream velocity is $U_\infty = 1$ m/s. Four different gases are released with varying densities but with the same vertical mass-flux, Q, from the source. Characteristics of the incoming boundary
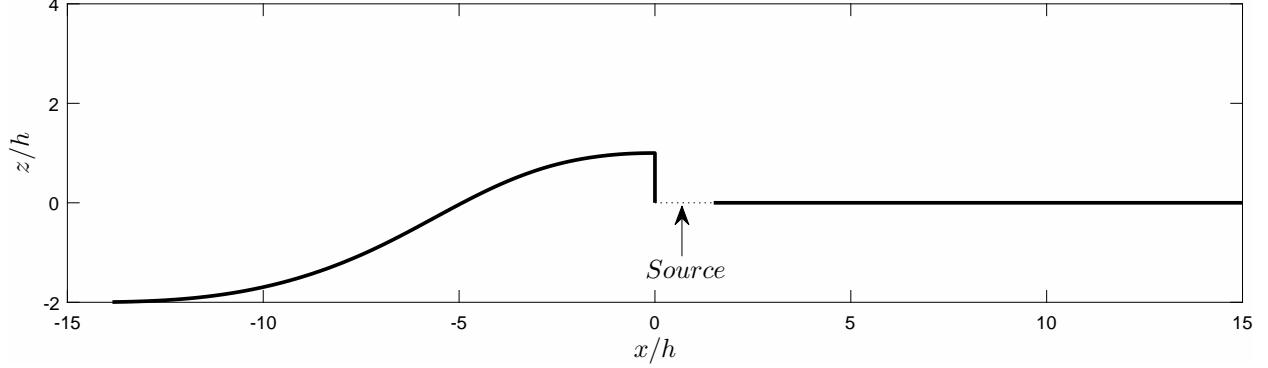
FIG. 1: Schematic illustration of the two-dimensional backward-facing step. The source location is marked with a dotted line.

layer and the source conditions are listed in Table I whereas the material properties of the different gases considered in this study are listed in Table II. The material properties of the non-neutral gases (cases 2–4) correspond to common TICs, namely carbon dioxide, sulphur dioxide, and chlorine gas, respectively. A simplifying assumption in the present study is that only isothermal conditions are considered. TICs are commonly stored in pressurized tanks from which a release would result in a gas phase that initially is much colder than the surrounding air. Despite this simplification the present study enables a systematic assessment of the effect of density differences on the dispersion process.

The friction velocity is defined as $u_\tau = \sqrt{\tau_w/\rho}$, where $\tau_w = \mu \partial_z U|_{wall}$ is the wall frictional stress, and the frictional Reynolds number is defined as $\mathrm{Re}_\tau = u_\tau H \rho / \mu$.

TABLE I: Incoming boundary-layer and source characteristics.

Parameter	Description	
H	Boundary-layer thickness	1 m
h	Back-step height	0.1 m
U_∞	Free-stream velocity	1 m/s
$\mathrm{Re}_\tau|_{x/h=-13.85}$	Frictional Reynolds number at inlet	2285
Δx	Source size in streamwise direction	0.15 m
Q	Emission rate	0.2682 kg/(m²s)

5

TABLE II: Material properties of the released gases for the four cases considered in this study. ρ_1, μ_1, ν_1, and α_1 denote properties of the neutral gas released in case 1.

Case	Density ρ [kg/m^3]	Dynamic viscosity μ [kg/(ms)]	Kinematic viscosity ν [m^2/s]	Molecular diffusion coefficient α [m^2/s]
1	1.1894	$1.8232 \cdot 10^{-5}$	$1.5329 \cdot 10^{-5}$	$1.9746 \cdot 10^{-5}$
2	$1.5 \times \rho_1$	$0.81 \times \mu_1$	$0.54 \times \nu_1$	$0.81 \times \alpha_1$
3	$1.9 \times \rho_1$	$0.69 \times \mu_1$	$0.36 \times \nu_1$	$0.61 \times \alpha_1$
4	$2.5 \times \rho_1$	$0.72 \times \mu_1$	$0.28 \times \nu_1$	$0.54 \times \alpha_1$

III. MODELLING

In this paper, Cartesian tensor notation and Einstein's summation convention are employed. Temporal and spatial gradients are denoted $\partial_t = \partial/\partial t$ and $\partial_i = \partial/\partial x_i = (\partial/\partial x, \partial/\partial y, \partial/\partial z)$, respectively. Furthermore, $(\bar{\cdot})$ and $(\tilde{\cdot})$ are used to denote filtered and Favre averaged quantities, respectively. These quantities are also referred to as the resolved fields.

A. Governing equations

The filtered equations governing the conservation of mass and momentum for a Newtonian fluid with variable density can be written as

$$\partial_t(\bar{\rho}) + \partial_j(\bar{\rho}\tilde{u}_j) = 0, \tag{1}$$

$$\partial_t(\bar{\rho}\tilde{u}_i) + \partial_j(\bar{\rho}\tilde{u}_i\tilde{u}_j) = -\partial_i\bar{p} + \partial_j(2\bar{\mu}\tilde{s}_{ij}) + \bar{\rho}g_i - \partial_j\tau_{ij}. \tag{2}$$

Here, $\tilde{u}_i(\mathbf{x}, t) = (\tilde{u}, \tilde{v}, \tilde{w})$ is the velocity, $\bar{p}(\mathbf{x}, t)$ is the pressure, and $g_i = (0, 0, -g)$ is the gravitational acceleration. The filtered density is defined as

$$\bar{\rho}(\tilde{\zeta}) = \frac{1}{\tilde{\zeta}\rho_i^{-1} + (1 - \tilde{\zeta})\rho_1^{-1}}, \tag{3}$$

where $\tilde{\zeta}(\mathbf{x}, t)$ is the mass fraction of gas in air and ρ_i is the gas density of case i. The filtered dynamic viscosity, $\bar{\mu}(\tilde{\zeta})$, is calculated in the same manner as $\bar{\rho}(\tilde{\zeta})$ and the trace-free

strain-rate tensor is given by

$$\tilde{s}_{ij} = \frac{1}{2}(\partial_j \tilde{u}_i + \partial_i \tilde{u}_j) - \frac{1}{3}\delta_{ij}\partial_k \tilde{u}_k. \tag{4}$$

The last term in (2) is the residual-stress tensor, $\tau_{ij} = \bar{\rho}(\widetilde{u_i u_j} - \tilde{u}_i \tilde{u}_j)$, which is modelled using an eddy-viscosity approach, i.e. $\tau_{ij} = -2\mu_t \tilde{s}_{ij}$. Here, the eddy viscosity, $\mu_t(\mathbf{x}, t)$, is calculated using the local dynamic Smagorinsky model with a least squares based filter. Details about LES theory and how to model the eddy-viscosity can be found in e.g. Gatski and Bonnet[16], Pope[17] and Lesieur, Métais, and Comte[18].

The filtered equation governing the transport of mass fraction of a scalar field is given by

$$\partial_t(\bar{\rho}\tilde{\zeta}) + \partial_j(\bar{\rho}\tilde{\zeta}\tilde{u}_j) = \partial_j\left(\bar{\rho}\alpha\partial_j\tilde{\zeta}\right) - \partial_j t_j, \tag{5}$$

where α is the molecular diffusion coefficient of the scalar field. The unresolved sub-grid scalar flux, $t_j = \bar{\rho}(\widetilde{u_j\zeta} - \tilde{u}_j\tilde{\zeta})$, is modelled similarly to the momentum sub-grid stresses, i.e. $t_j = -(\mu_t/Sc_t)\partial_j\tilde{\zeta}$. In this study the turbulent Schmidt number is set to $Sc_t = 0.9$, a value corresponding to what is commonly used in the literature[19]. The volume concentration of a released gas is calculated as (c.f. (3))

$$\tilde{c}(\tilde{\zeta}) = \frac{\tilde{\zeta}}{\rho_i}\bar{\rho}(\tilde{\zeta}). \tag{6}$$

The limiting behavior $\tilde{c}(\tilde{\zeta} = 1) = 1$ thus corresponds to the condition at the source location.

B. Statistical measures

The resolved fields can be decomposed into a mean and a fluctuating part, i.e. $\tilde{u}_i = U_i + u_i$, $\tilde{c} = C + c$, and $\bar{p} = P + p$. Here, the upper-case symbols represent averaged fields whereas the lower-case symbols denote fluctuations. Averaged quantities are averaged both in time and the spanwise direction, e.g. for the velocity

$$U_i(x, z) = \langle \tilde{u}_i(\mathbf{x}, t) \rangle = \frac{1}{L_y T_{av}} \int_0^{L_y} \int_0^{T_{av}} \tilde{u}_i(\mathbf{x}, t)\mathrm{d}y\mathrm{d}t, \tag{7}$$

where $\langle \cdot \rangle$ denotes the averaging operator and L_y and T_{av} the averaging length and time, respectively. All root-mean-square variables, denoted with the subscript rms, are defined

as the square root of the auto-correlation of that variable. Furthermore, the correlation coefficient between two variables, say u_i and u_j, is defined by

$$\rho_{ij} = \frac{\langle u_i u_j \rangle}{\sqrt{\langle u_i^2 \rangle \langle u_j^2 \rangle}}, \tag{8}$$

where there is no summation of repeated indices.

The most commonly used statistical measures in turbulent flows are the Reynolds stress, $\langle u_i u_j \rangle$, and the turbulence kinetic energy, $k = 0.5 \langle u_i u_i \rangle$. The mean kinetic energy is similarly defined as $K = 0.5 U_i U_i$. It should be noted that the present Reynolds stress tensor is based on the Reynolds decomposition of the Favre filtered field and not on a regular Reynolds decomposition. The same is true for all other statistical measures based on the velocity and scalar fields. Previous studies have shown that this is an acceptable approximation, see Wingstedt *et al.*[14].

C.   Turbulence structure tensors

Single-point turbulence structure tensors can be used to elucidate the energetic large-scale structures of turbulent flows. Their definitions are based on the turbulence stream function, ψ_i, defined by

$$u_i = \epsilon_{ijk} \partial_j \psi_k, \qquad \partial_i \psi_i = 0, \qquad \partial_k \partial_k \psi_i = -\omega_i. \tag{9}$$

Here, u_i and ω_i are the fluctuating parts of the turbulent velocity and vorticity fields, respectively, and ϵ_{ijk} is the cyclic permutation tensor. The fluctuating velocity field is assumed to be divergence-free which is an approximation for the variable density formulation used in this study. However, based on the reconstructed velocity field from the stream function the approximation seems to be valid. The stream function is calculated using the method of Stylianou, Pecnik, and Kassinos[20].

Following Kassinos, Reynolds, and Rogers[21], one-point correlation tensors carrying non-

local information are defined from products of the stream-function gradients:

$$R_{ij} = \langle u_i u_j \rangle = \epsilon_{ikl}\epsilon_{jmn}\langle \partial_k \psi_l \partial_m \psi_n \rangle, \hspace{3cm} \text{(Componentality)}$$

$$D_{ij} = \langle \partial_i \psi_k \partial_j \psi_k \rangle, \hspace{3cm} \text{(Dimensionality)}$$

$$F_{ij} = \langle \partial_k \psi_i \partial_k \psi_j \rangle, \hspace{3cm} \text{(Circulicity)}$$

$$C_{ij} = \langle \partial_k \psi_i \partial_j \psi_k \rangle. \hspace{3cm} \text{(Inhomogeneity)}$$

The different structure tensors carry complementary statistical information about the turbulence. It should be noted, however, that these are not linearly independent tensors. The componentality, or Reynolds stresses, gives information about the amplitude of the different components of the fluctuating velocity field. The dimensionality tensor carries information about the spatial extent of the turbulence structures and reveals the level of two-dimensionality of the turbulence field. The circulicity tensor is a measure of the large-scale structures in the vorticity field and a large value of F_{ij} indicates the presence of 'vortical' eddies. Finally, the inhomogeneity tensor represents the deviation from a homogeneous state of turbulence; it can be shown that C_{ij} is identically zero for homogeneous turbulence. More detailed physical interpretations of the structure tensors can be found in e.g. Kassinos, Reynolds, and Rogers[21], Kassinos[22] and Bhattacharya, Kassinos, and Moser[23].

D.   Numerical formulation

The numerical simulations are conducted using the low-Mach, variable-density solver VIDA developed by Cascade Technologies. This is an unstructured, finite-volume based solver with a low-dissipation numerical scheme. VIDA is up to second order in space and time. For more information about the numerical method, see e.g. Pierce and Moin[24], Ham and Iaccarino[25], Ham, Mattsson, and Iaccarino[26] and Ham[27].

The computational domain is periodic in the spanwise direction. A no-slip boundary condition is used at the ground whereas the top uses a slip condition. The grid consists of approximately 6.8×10^6 hexahedral cells where the cell density is highest in the vicinity of the source and the backward-facing step. Characteristics of the computational resolution are summarized in Table III. It should be noted that the same computational mesh is used

for all cases but since the kinematic viscosity depends on the release the friction velocities change too; hence the plus-units differ between the cases.

A CFL criterion of 0.7 has been used to determine the time step for all simulations. This results in an average time step of approximately 0.0007 s in all cases. For the averaging times employed here (see Table III), this results in simulation times of approximately two weeks on 120 computational cores.

TABLE III: Characteristics of the computational resolution and averaging time. (N_x, N_y, N_z) denotes the number of computational nodes in each direction and x^+, y^+, and z^+ are the collocation resolution at the wall normalized by the viscous length scale ν/u_τ. $l^+ \approx \sqrt[3]{V_{cell}}\sqrt{|S|/\nu}$ is a non-dimensional length scale and T_{AV} is the averaging time.

Case	(N_x, N_y, N_z)	(x^+_{min}, x^+_{max})	(y^+_{min}, y^+_{max})	(z^+_{min}, z^+_{max})	(l^+_{min}, l^+_{max})	T_{AV} [s]
1	(245,350,90)	(2.2, 107.4)	(12.0, 26.1)	(2.2, 4.7)	(0.85, 44.0)	315
2	(245,350,90)	(3.8, 54.4)	(13.2, 23.9)	(2.4, 4.3)	(0.70, 43.2)	200
3	(245,350,90)	(6.4, 63.8)	(15.5, 35.5)	(2.8, 6.5)	(0.89, 44.0)	190
4	(245,350,90)	(7.4, 82.2)	(20.0, 40.6)	(3.6, 7.4)	(0.62, 48.5)	230

The inflow conditions for LES should reflect the three-dimensional, unsteady nature of turbulence in order to achieve physically realistic results. Here, the inflow turbulence is identical to that used in Wingstedt *et al.* [14] which was designed to match the experimental conditions in an atmospheric wind tunnel at similar Reynolds number. It is based on a separate precursor simulation with periodic side walls and roughness elements placed staggered on the ground, c.f. Wingstedt *et al.* [14] for more details. At the downstream boundary, an outflow boundary condition is used.

IV. RESULTS AND DISCUSSION

Figure 2 shows the development of the frictional Reynolds number downstream the source for the different cases considered in this study. The regions where $Re_\tau \leq 0$ indicate the presence of a recirculation zone, which is seen to decrease as density increase. Further downstream the source, the frictional Reynolds number stabilizes and is more similar to a developing three-dimensional turbulent boundary layer. Significant variation of Re_τ can be observed depending on the density difference of the emitted gas.
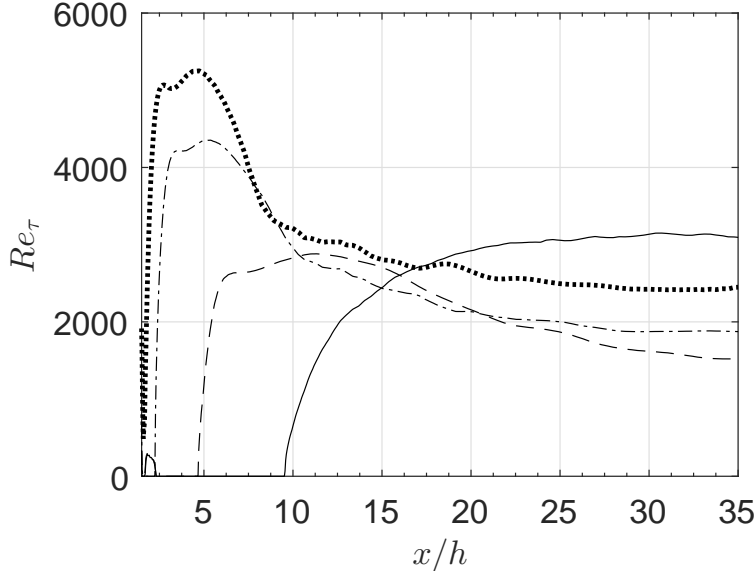
FIG. 2: Downstream development of Re_τ for cases 1 (——), 2 (– – –), 3 (– · –), and 4 (······).

The main focus of attention in this paper is the almost fully developed flow region ($x/h > 20$) where the influence of the source can be assumed to be small. However, the flow characteristics in the vicinity of the source will first briefly be discussed.

Figure 3 illustrates of the mean velocity field close to the source for cases 1 and 3 using the line-integral convolution (LIC) technique[28]. For the neutral release, the source pushes the recirculation zone further away from the back-step compared to a flow field without a release[29]. Also, the flow passing over the back-step is slightly deformed and moved upwards. The dense gas source does not penetrate the free-stream as much. It can also be seen that there is only a very small recirculation zone in the immediate vicinity of the source. The near source region of the densest gas greatly resembles case 3, only that the gas does not reach the top of the back-step, whereas case 2 is more similar to the neutral case with a recirculation region that reaches $x/h \approx 5$ and a somewhat penetrated free-stream.

Figure 4 shows a visualization of instantaneous concentration gradients for cases 1 and 3, taken in a plane in the middle of the computational domain. In the neutral release (Figure 4a) it is seen that air is entrained already at the end of the source ($x/h = 1.5$). The flow is well mixed with no sharp concentration gradients downstream approximately $x/h = 5$. In the dense gas case (Figure 4b), instabilities similar to Kelvin-Helmholtz and Holmboe are observed above the source at the height of the back-step and the concentration gradient is found to be strongest in these billows. The instabilities also seem to generate an oscillating
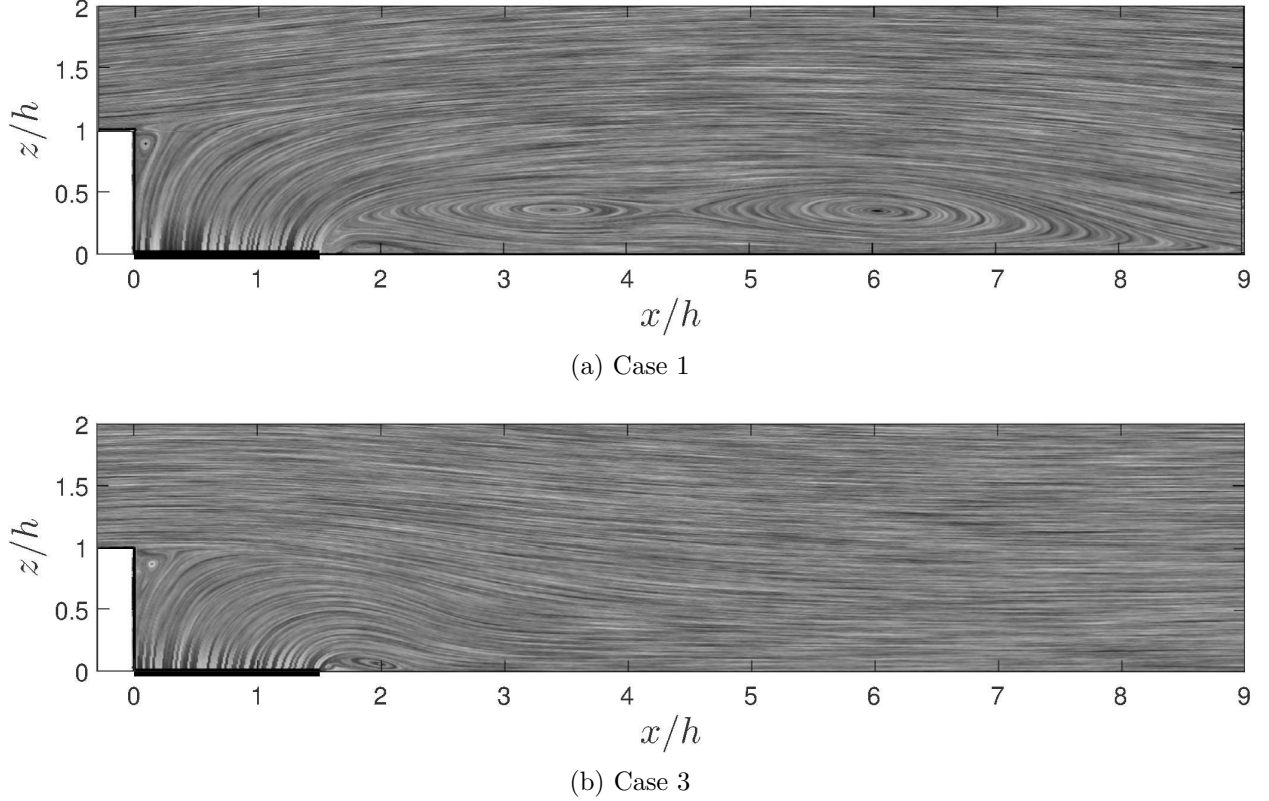
11

(a) Case 1

(b) Case 3

FIG. 3: Mean velocity field close to the source for cases 1 and 3 visualised using LIC. The black line at $0 \leq x/h \leq 1.5$ shows the source location and the white area $(x/h \leq 0)$ is the backward-facing step.

interphase visible further downstream $(x/h \gtrsim 6)$, where relatively strong gradients are still present.

A. Downstream region

The results presented in this section are taken at the downstream position $x/h = 26$ where the wall quantities are according to Table IV. As seen in Figure 2, the frictional Reynolds number has almost stabilized at this point, which indicates that the local effect of the source dynamics and the back-step no longer dominate the flow field.

1. Mean flow and dispersion characterization

Figure 5 shows the vertical variation of normalized mean streamwise velocity. Clear differences between case 1 and the dense gas cases can be observed. Most notable is the
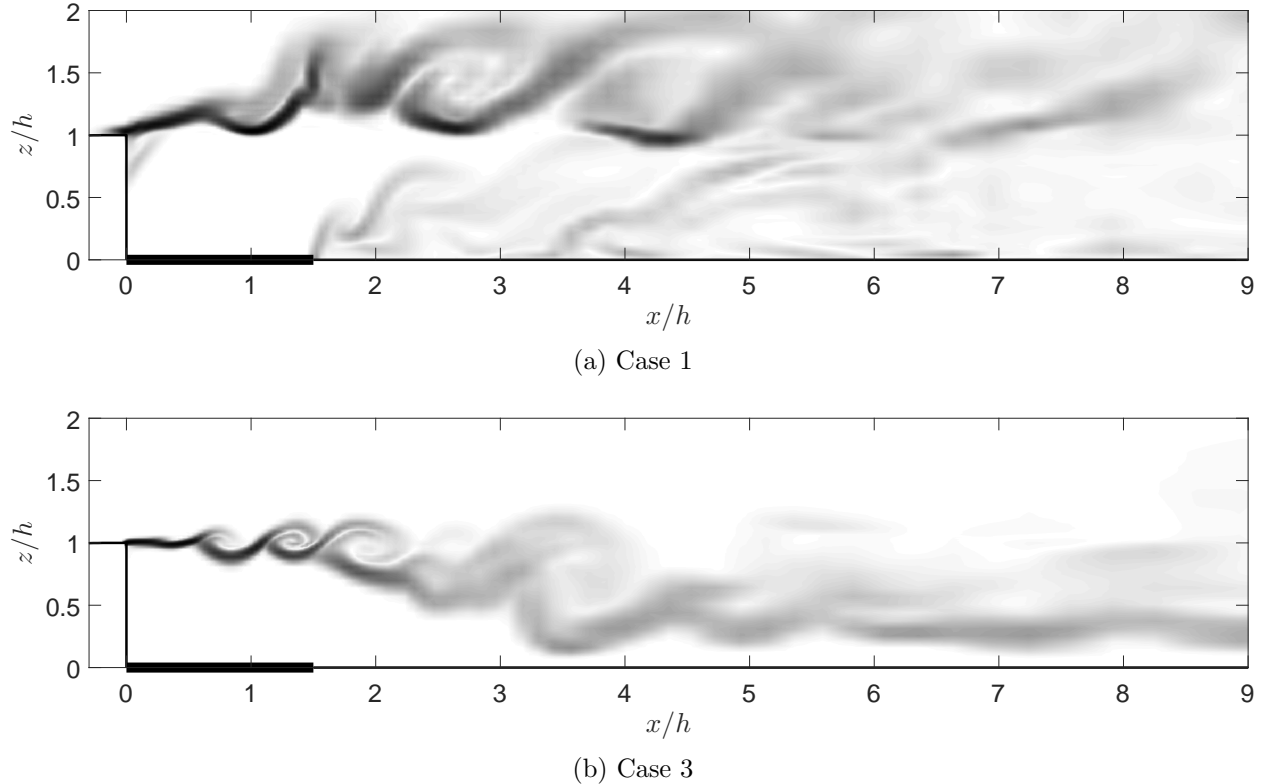
(a) Case 1

(b) Case 3

FIG. 4: Numerical Schlieren visualization[30] of concentration gradients, $e^{-\chi}$ where $\chi = \frac{5|\nabla \tilde{c}|}{|\nabla \tilde{c}|_{max}}$, for cases 1 and 3. The thick black lines on the x−axis represent the source location.

TABLE IV: Wall quantities for the four cases considered in this study at $x/h = 26$.

Case	Friction velocity u_τ [m/s]	Frictional Reynolds number Re_τ [−]
1	0.047	3070
2	0.015	1800
3	0.011	1960
4	0.011	2480

significant reduction close to the ground in the dense-gas cases, followed by an increase further away from the wall. This is consistent with experimental findings[15,31]. The straight thick line in the figure corresponds to a logarithmic profile. In the neutral case, the mean velocity exhibits a logarithmic variation in the region $0.1 \leq z/h \leq 0.5$ which corresponds to $32 \leq z^+ \leq 155$. The mean velocity profiles for the dense gas cases appear to be shifted outwards but nevertheless show a logarithmic behaviour in the region $2 \lesssim z/h \lesssim 5$, corresponding

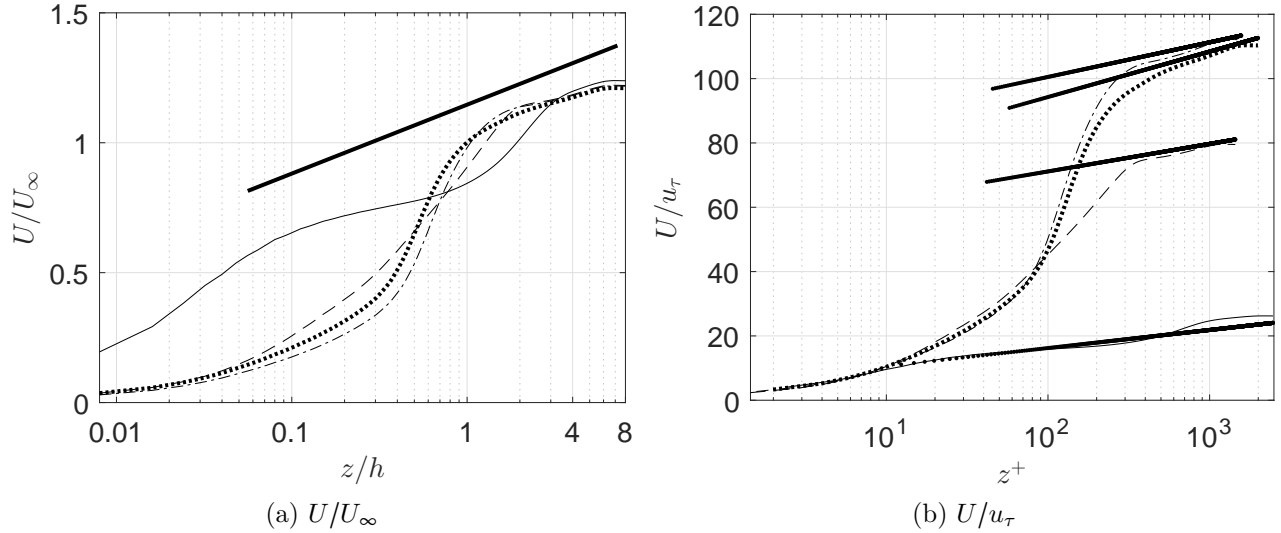13

roughly to $360 - 500 \lesssim z^+ \lesssim 900 - 1250$.

(a) U/U_∞ (b) U/u_τ

FIG. 5: Mean velocities for cases 1 (——), 2 (– – –), 3 (– · –), and 4 (· · · · · ·). The thick line (——) shows a logarithmic behaviour.

Figure 6 displays the predicted variation of the mean and fluctuating concentrations, scaled by the source concentration ($C^* = 1$). Figure 6a shows that the mean concentration for case 2, i.e. the least dense gas, is approximately 90 % of the source concentration close to the wall at this downstream position. This indicates air entrainment throughout the entire plume. The two densest plumes (cases 3 and 4) have only partially been entrained by air since the source concentration is retained in a layer closest to the wall. For the neutral case, the maximum concentration is approximately 20 % of the source concentration, indicating a well-mixed field at this location. The plume thickness for the neutral and dense cases at this downstream position is approximately $z/h \approx 3.7$ and $z/h \approx 1.2 - 1.9$, respectively.

The fluctuating concentration displayed in Figure 6b exhibits its maximum value in close proximity to the position of maximum mean scalar gradient for all four cases. The peak fluctuations are increased for all the dense gases and they are also located closer to the wall compared to the neutral case, where the peak is located above the back-step height.

Density stratification caused by the rapid variation of density across the dense plume in the presence of mean shear may cause significant changes of turbulence intensities and structures. This has the potential to alter the momentum exchange between the plume and the outer region of the flow field. The stratification caused by the imposed density variation in the direction of gravity can locally be both stable and unstable depending on the plume
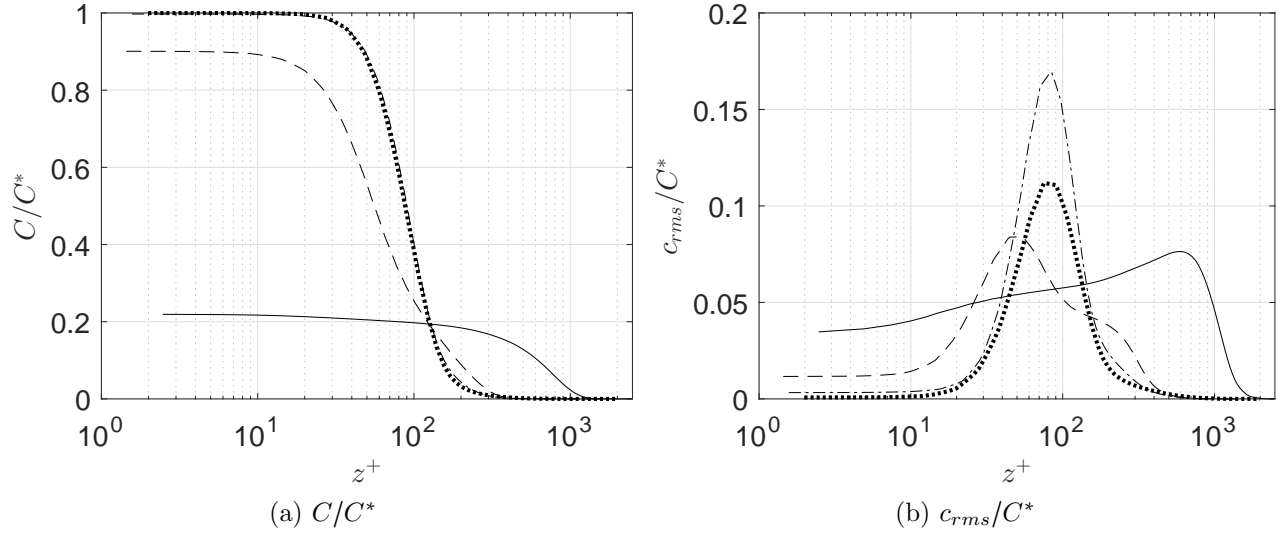
14

FIG. 6: Mean and rms concentrations normalized by the source concentration for cases 1 (——), 2 (– – –), 3 (– · –), and 4 (·······). Note the different values on the y-axis.

shape, location, and gas concentration.

The impact of stratification on the turbulence is commonly characterized by the gradient Richardson number given by $\mathrm{Ri}_g = N^2/S^2$, where $N = \sqrt{-g\rho_1^{-1}\partial_z\rho}$ is the Brunt-Väisälä frequency and $S = \sqrt{2S_{ij}S_{ij}}$ is the norm of the mean strain-rate tensor. It should be noted that Ri_g is generally a local variable that depends on both time and spatial position, whereas in this study $\mathrm{Ri}_g(x, z)$. It is commonly assumed that if the gradient Richardson number exceeds a critical value the flow field is locally stable in which the turbulence is significantly suppressed. Accepted range of this critical number varies between 0.2 and 1. Figure 7a shows the vertical variation of the gradient Richardson number. Interestingly, all cases show a clear double-peak behaviour indicating significant variation of the stratification across the plume. The stability increases monotonically with increased plume density near the wall whereas the opposite trend is observed further out in the domain. The results show the existence of a narrow layer within the plume itself ($120 \lesssim z^+ \lesssim 250$) where the impact of stable stratification can be expected to be reduced. The sensitivity of the results with respect to plume density thus suggests that the downstream development of turbulence in dense plumes may vary significantly with moderate changes of gas concentrations.
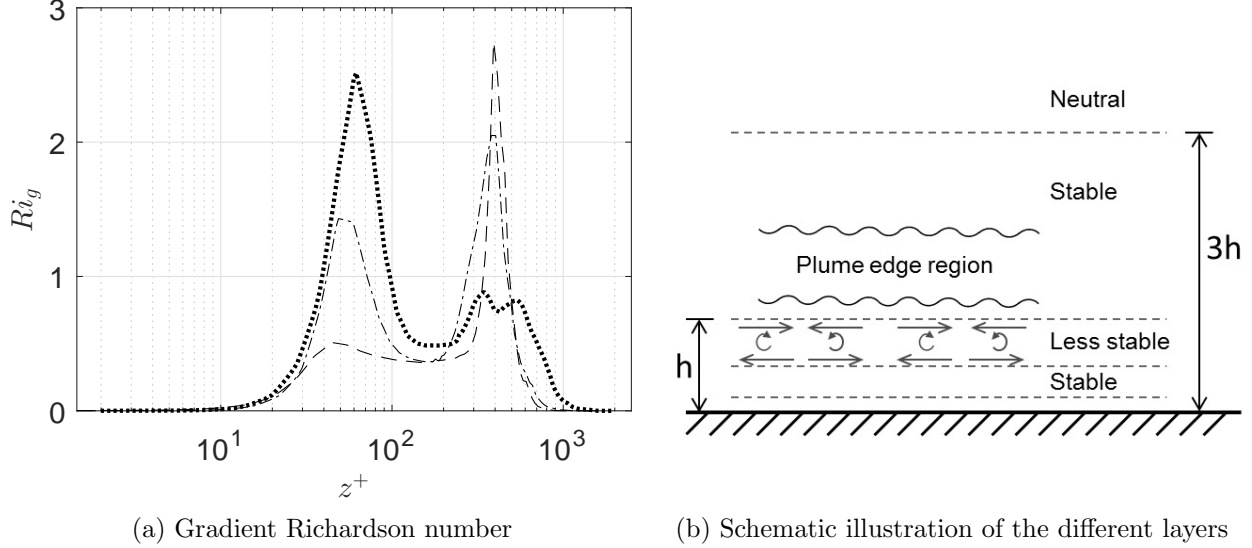
15

(a) Gradient Richardson number

(b) Schematic illustration of the different layers

FIG. 7: Vertical variation of the gradient Richardson number for cases 2 ($---$), 3 ($-\cdot-$), and 4 ($\cdots\cdots$) together with a schematic illustration of the stable layers.

2. *Turbulence dynamics and structures*

The momentum exchange between the mean and turbulence flow fields can be assessed using the turbulence structure parameter, $\langle uw \rangle/k$, which in equilibrium turbulent boundary layers is approximately 0.3 (Bradshaw[32]). The results displayed in Figure 8a is consistent with this but, more interestingly, the dense-plume results indicate a significant reduction of momentum exchange, in fact almost entirely annihilated in the inner part of the plume ($z^+ \lesssim 100 - 150$). The momentum exchange then increases, approaching a peak value of approximately 0.25 outside of the plume. It should be noted that for case 2 (the least-dense plume) there is a tendency for a secondary peak to develop closer to the wall compared to cases 3 and 4. This seems consistent with the observation made in Figure 7a, namely that the region in between the Ri_g peaks extends further out in case 2 which implies that the flow locally is less stable in this case compared to the other two dense-gas cases. The variation of the turbulence-to-mean kinetic energy is shown in Figure 8b. Apart from the near-wall region ($z^+ \lesssim 100$), the turbulence to mean kinetic energy is significantly reduced for the dense gas cases, which support the previous observation of reduced momentum exchange.

The profound effects on the turbulence field imposed by the stably stratified dense plumes are also clearly visible in Figure 9 where the normalized streamwise $\langle uu \rangle$, wall-normal $\langle ww \rangle$, and shear $\langle uw \rangle$ Reynolds stress components are shown. The near-wall behaviour of $\langle ww \rangle$ is
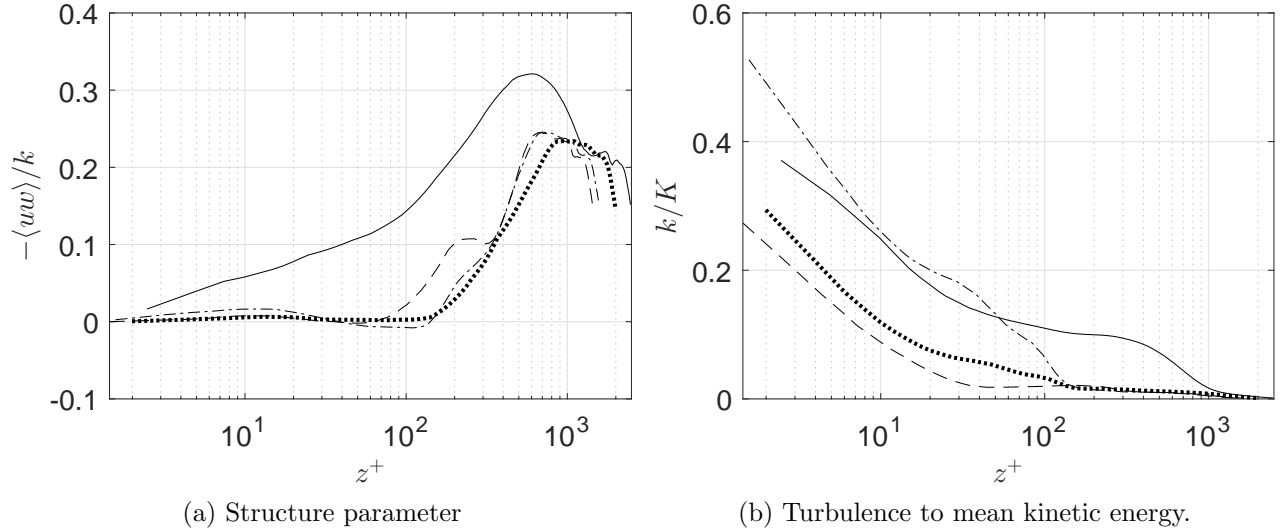
16

(a) Structure parameter (b) Turbulence to mean kinetic energy.

FIG. 8: Vertical variation of the structure parameter and kinetic energy for cases 1 (——), 2 (– – –), 3 (– · –), and 4 (·······).

significantly altered in all dense-plume cases whereas the outer peak is increased compared to case 1. It should, however, be noted that this is an effect of the friction velocity scaling and that the non-normalized wall-normal stresses are suppressed compared to the neutral case.

The shear component of the Reynolds stress tensor is important for production of turbulence kinetic energy in this case. As seen in Figure 9c, $\langle uw \rangle$ is dampened close to the wall for all dense gas cases compared to the neutral case. For case 3, momentum flux reversal, i.e. $\langle uw \rangle > 0$, is visible in the area $40 \lesssim z^+ \lesssim 150$, which indicates negative shear production of turbulence kinetic energy.

The streamwise Reynolds stresses are also significantly altered in cases 2–4 compared to the neutral case. In the two densest cases (3 and 4), a narrow peak appear at $z^+ \approx 100$. At the same location there is no correlation to the wall-normal fluctuations (c.f. Figure 9c). This behaviour is commonly seen in interfacial wave motions[33].

The predicted variation of vertical scalar flux is shown in Figure 10. It is seen that $\langle cw \rangle$ is significantly reduced across the inner layer of the dense plumes where even scalar flux reversal can be observed in the same region as momentum flux reversal occurs in Figure 9c for case 3. This implies that also the buoyancy production is negative and that energy is extracted from the turbulence to the mean field. It should be noted that both momentum and scalar flux reversal also occurs for case 4 at different downstream positions.
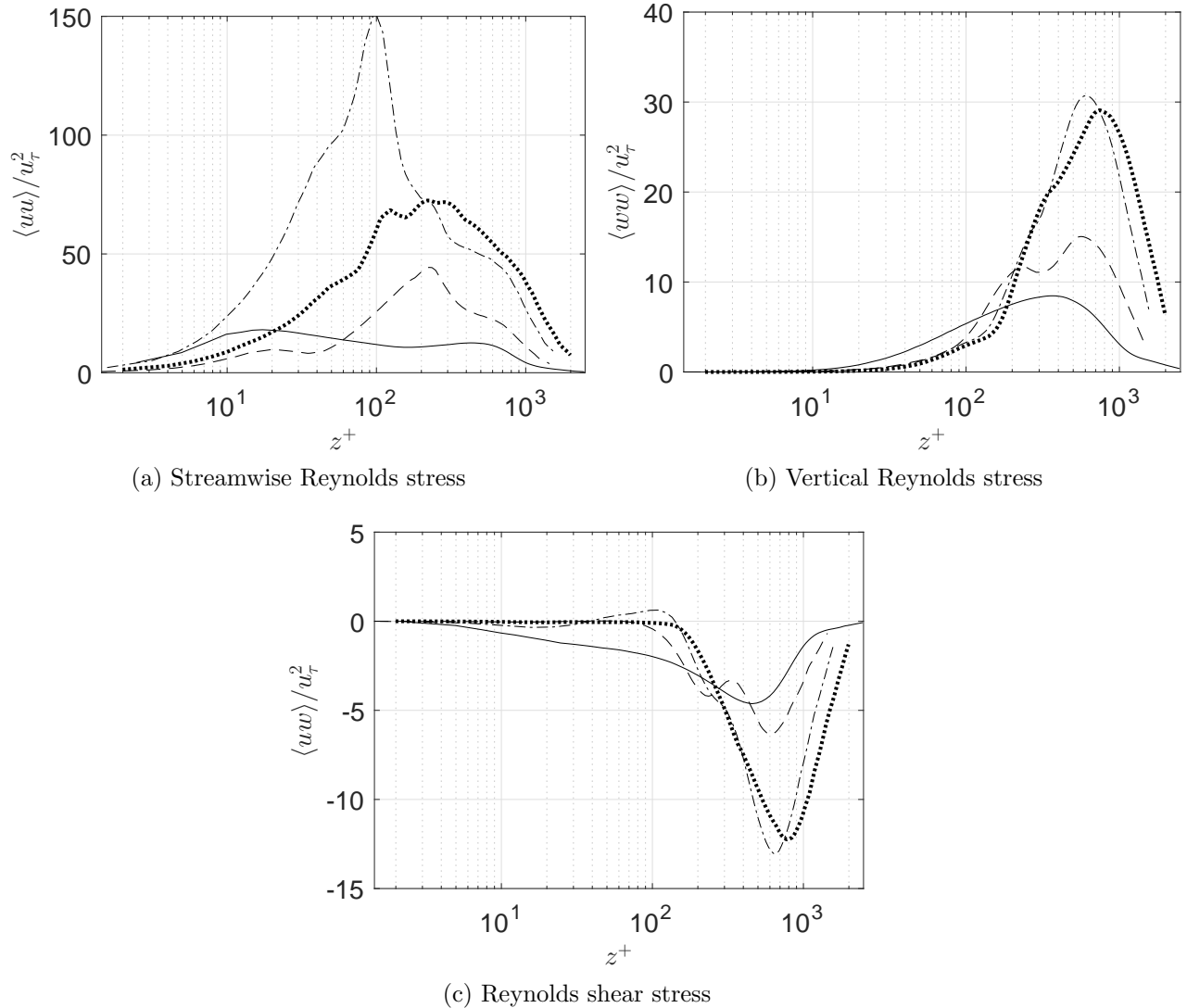
(a) Streamwise Reynolds stress

(b) Vertical Reynolds stress

(c) Reynolds shear stress

FIG. 9: Reynolds stress components normalized by each case respective friction velocity (see Table IV). The lines represent cases 1 (——), 2 (– – –), 3 (– · –), and 4 (·······).

The correlation coefficient for streamwise scalar flux, found in Figure 11, shows a near perfect negative correlation for cases 3 and 4 in the region around $z^+ \approx 100$, which coincides with the peak in $\langle uu \rangle$. This further corroborates the observation that the fluctuations closely resemble interfacial wave modes.

Figure 12 shows the turbulence to mean flow and turbulence to buoyancy time scales. In equilibrium boundary layers, $Sk/\varepsilon \approx 5$, which is clearly not the case for the present dense-gas simulations. Furthermore, as the turbulent time scale becomes much larger than both the mean flow and buoyancy time scales, relaminarization of the flow field is occurring. Hence, it is likely that the interfacial wave modes are dampened. It should be noted that both
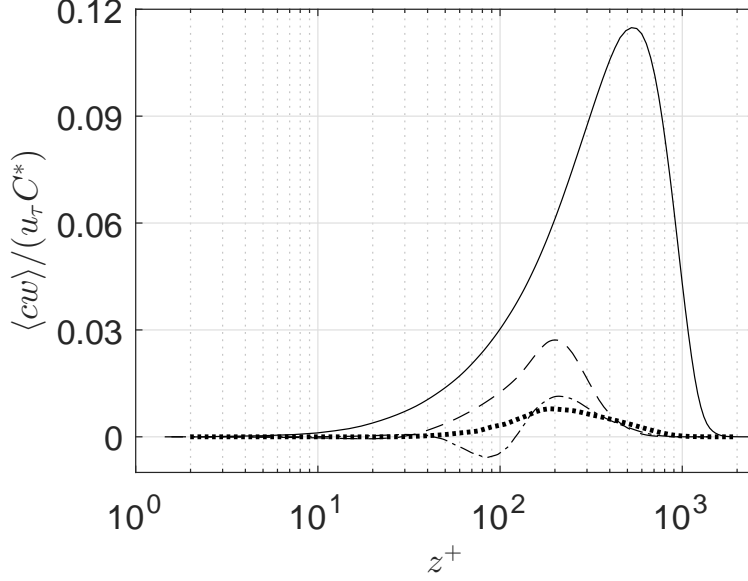
FIG. 10: Wall-normal scalar-flux component normalized by the source concentration and the friction velocity of each case (see Table IV). The lines represent cases 1 (——), 2 (– – –), 3 (– · –), and 4 (·······).
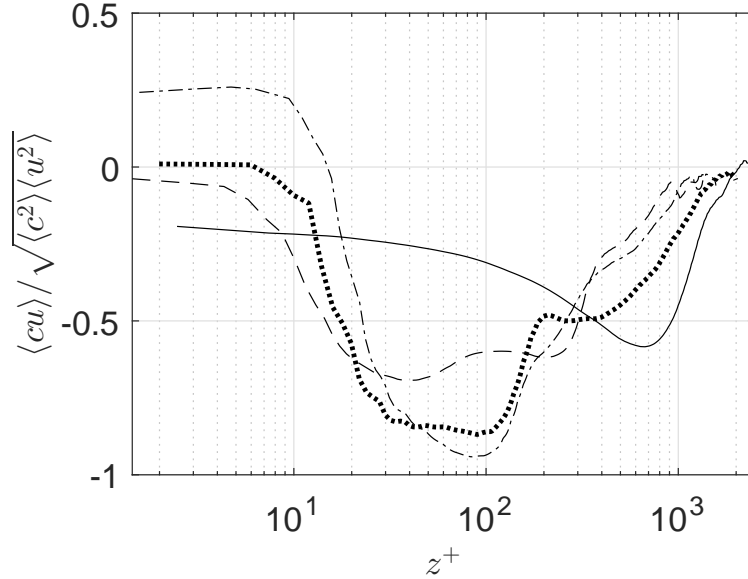

FIG. 11: Vertical variation of the correlation coefficient of streamwise velocity and scalar field for cases 1 (——), 2 (– – –), 3 (– · –), and 4 (·······).

interfacial waves and relaminarization processes involve time scales that can be significantly longer than those of equilibrium turbulence. While this has been taken into account by considering long averaging times, the ergodicity assumption involved in obtaining the present statistics can be questioned.

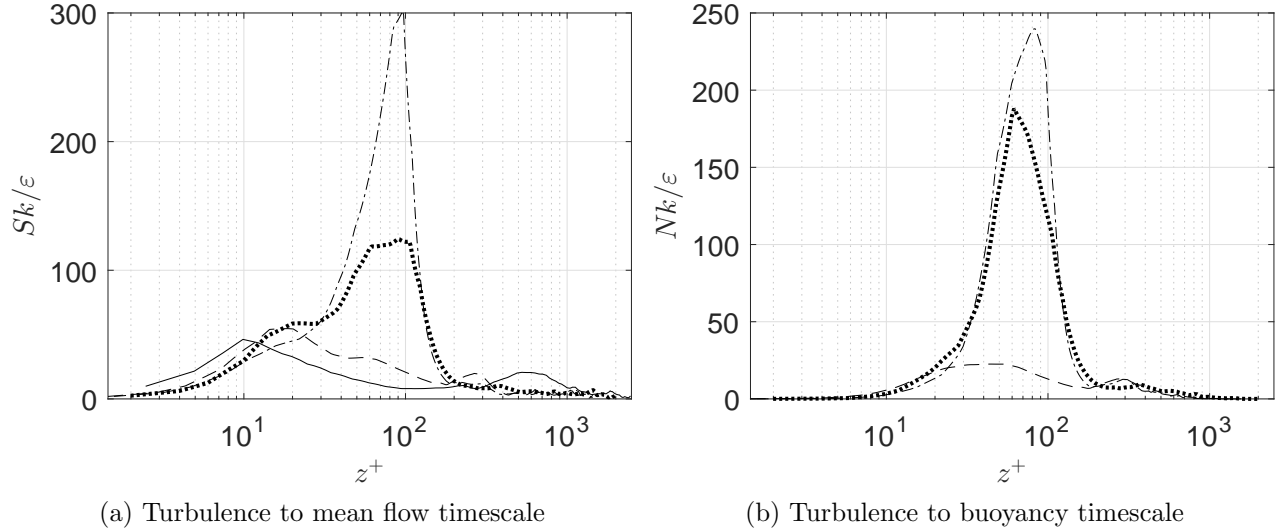The dispersion process is highly dependent on the energy-containing large-scale motion of

19

(a) Turbulence to mean flow timescale   (b) Turbulence to buoyancy timescale

FIG. 12: Vertical variation of time scales for cases 1 (——), 2 (– – –), 3 (– · –), and 4 (·······).

the flow field. The large-scale turbulence motion is, however, inadequately described by only the Reynolds stresses[21]. To further characterize the field the dimensionality and circulicity tensors , described in Section III C, are investigated.

Figure 13 shows the vertical variation of the normalized dimensionality components, emphasizing the 'geometrical' aspect ratio of the average turbulence structures, for the four cases. It is seen that the dimensionality far from the wall is very similar in all cases, with tube-like structures ($D_{11} < D_{22} \approx D_{33}$), consistent with what is seen in a plane channel flow. Also, very close to the wall, the structures are relatively similar in all cases, elongated in the streamwise direction compared to the wall-normal ($D_{33}/D_{11} \approx 8 - 10$), which is consistent with near-wall streaks[34]. The neutral case exhibits extremal points around $z^+ = 20$, the same as in a plane channel[35], whereas in the densest cases these points are moved further out in the boundary layer to approximately $z^+ = 100$.

The largest difference in dimensionality between neutral and dense gas releases is found around $z^+ \approx 100$, which coincides with the extremal point for the streamwise Reynolds stress, and the transition from the inner to the middle layers (see Figure 7a). At this location, the densest cases show $D_{11} < D_{22} << D_{33}$ indicating that the structure have a limited wall-normal extension and longer coherence length in the streamwise direction compared to the spanwise direction. Hence, the structures are very compressed in the vertical direction and stretched in both spanwise and streamwise directions and may be described as elongated pancakes.

The circulicity tensor components, seen in Figure 14, yield information about the energy-
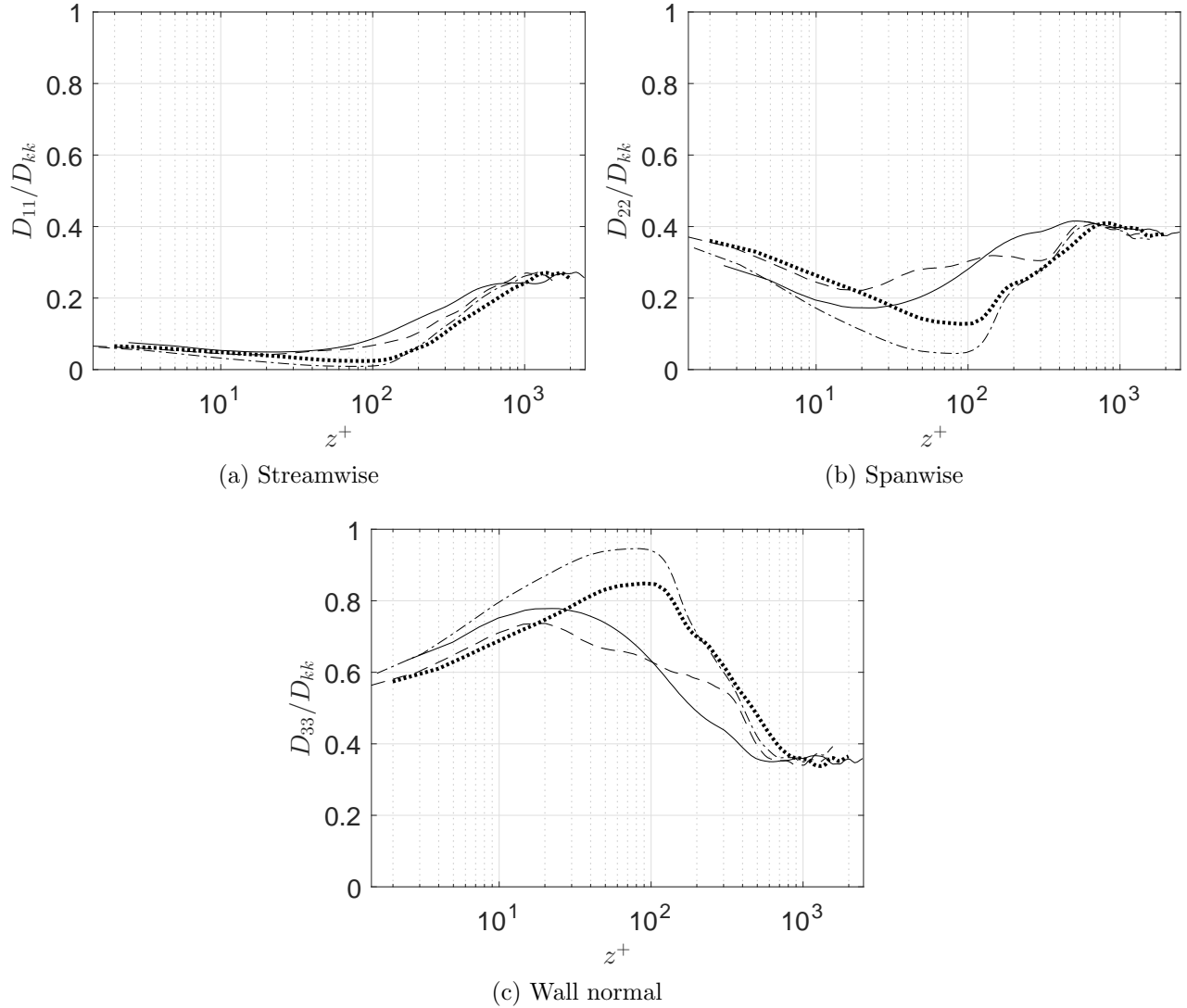
20

(a) Streamwise

(b) Spanwise

(c) Wall normal

FIG. 13: Components of the normalized dimensionality tensor for cases 1 (——), 2 (– – –), 3
(– · –), and 4 (·······).

containing vortical structure. Case 1 shows similar behaviour as turbulent channel flow, especially far from the wall. The spanwise component, F_{22}, deviates the most compared to channel flow and shows a deficit of 0.15 at the extremal point. This deficit is approximately equally distributed on the other two components.

For cases 3 and 4, the maximum deviation from the neutral case is found around $z^+ \approx 100$. At this position the circulicity tensor exhibits significant anisotropy, not seen in case 1, and the normalized spanwise circulicity increases significantly at the expense of the other two components. This indicates that in the case of dense gas release rotation about the spanwise axis is promoted, a feature that has also been observed in stably stratified channel flow[36]. A

possible explanation for this is the generation of waves, comprising of rolling motion around the y-axis, which is also consistent to the relatively sharp peaks found in all the circulicity components.
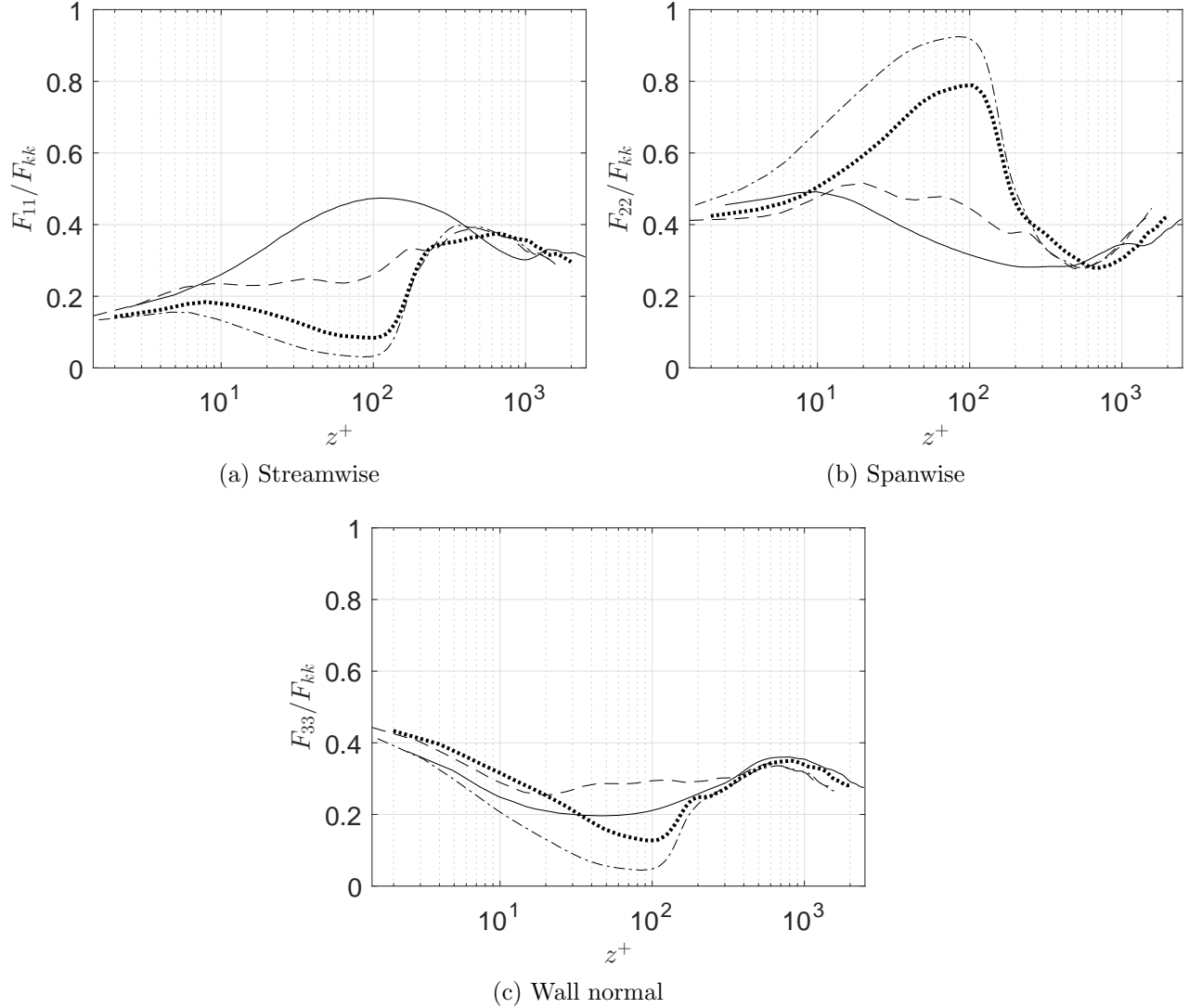

(a) Streamwise

(b) Spanwise

(c) Wall normal

FIG. 14: Components of the normalized circulicity tensor for cases 1 (——), 2 (– – –), 3 (– · –), and 4 (·······).

V.   CONCLUDING REMARKS

LES simulations of flow over a backward-facing step with dispersion of four gases with increasing densities have been performed and analysed with particular emphasis on the phase where the local effect of the source dynamics is no longer dominating the flow field.

The density of the released dense gases corresponds to the common TICs: carbon dioxide, sulphur dioxide, and chlorine gas, which are approximately 1.5, 2, and 2.5 times heavier than air, respectively.

Results show that the source alters the flow field differently for the different cases. The neutral release extends the recirculation region and deforms the flow passing over the back-step whereas the most dense releases only affect the flow field below the step height and almost eliminates the recirculation zone. The same concentration level as released at the source are found close to the wall at the investigated downstream position for cases 3 and 4 (i.e. the most dense cases), indicating that no air has managed to entrain the gases. It is also found that the vertical mixing is significantly reduced close to the wall for all dense gas releases compared to the neutral case.

By examining the gradient Richardson number, it is observed that all the dense gases are significantly affected by buoyancy in a large part of the domain. Interestingly, there exists a narrow layer within the plume where the impact of stratification is expected to be reduced. Both momentum and scalar flux reversal are found for case 3, indicating a negative shear and buoyancy production of turbulence kinetic energy and that energy is taken from the turbulence to the mean flow. The same feature has been observed also for case 4 but at different downstream locations. Turbulence-to-mean and turbulence-to-buoyancy time scales are found to be significantly larger for the two densest cases in the region where the gradient Richardson number is highest. In all, this suggests that a relaminarization process is occurring.

Interestingly, even though the flow field seems to be undergoing relaminarization, the densest cases show a high and narrow peak in streamwise Reynolds stress. In the same area, there is almost a perfect negative correlation between the flow field and the scalar field, which suggest that the fluctuations may be due to interfacial wave modes rather than turbulence. This is also corroborated by the density-gradient visualization where typical Kelvin-Helmholtz or Holmboe instabilities are developed close to the source and which may generate waves.

The large-scale structures have been examined within the dispersed plume. Significant changes occur with increased plume density, especially in the middle layer. At this location, the structures become more pancake-shaped and are elongated in the streamwise direction, compared to the neutral case where they can be described as somewhat flattened rods.

23

The large-scale vorticity is seen to be shifted to almost exclusively promote rotation about the spanwise axis in the dense gas cases. This is yet another indication of the presence of interfacial waves modes, where the waves comprise rolling motion about the spanwise axis.

ACKNOWLEDGMENTS

REFERENCES

[1] M. A. McBride, A. B. Reeves, M. D. Vanderheyden, C. J. Lea, and X. X. Zhou, "Use of advanced techniques to model the dispersion of chlorine in complex terrain," Process Safety Environment **79**, 89–102 (2001).

[2] G. A. Perdikaris and F. Mayinger, "Numerical simulation of heavy gas cloud dispersion within topographically complex terrain," Journal of Loss Prevention in the Process Industries **7**, 391–396 (1994).

[3] S. Sklavounos and F. Rigas, "Validation of turbulence models in heavy gas dispersion over obstacles," Journal of Hazardous Materials **A108**, 9–20 (2004).

[4] S. Tauseef, D. Rashtchian, and S. Abbasi, "CFD-based simulation of dense gas dispersion in presence of obstacles," Journal of Loss Prevention in the Process Industries **24**, 371–376 (2011).

[5] W. Coirier, D. Fricker, M. Furmanczyk, and S. Kim, "A Computational Fluid Dynamics approach for urban area transport and dispersion modeling," Environmental Fluid Mechanics **5**, 443–479 (2005).

[6] F.-S. Lien and E. Yee, "Numerical modelling of the turbulent flow developing within and over a 3D building array, Part I: A high-resolution Reynolds-Averaged Navier-Stokes approach," Boundary-Layer Meteorology **112**, 427–466 (2004).

[7] F.-S. Lien, E. Yee, H. Ji, A. Keats, and K. J. Hsieh, "Progress and challenges in the development of physically-based numerical models for prediction of flow and contaminant

dispersion in the urban environment," Int. Journal of Computational Fluid Dynamics **20**, 323–337 (2006).

[8]J. L. Santiago, A. Martilli, and F. Martín, "CFD simulation of airflow over a regular array of cubes. part i: Three-dimensional simulation of the flow and validation with wind-tunnel measurements," Boundary-Layer Meteorology **122**, 609–634 (2007).

[9]V. Boppana, Z.-T. Xie, and I. P. Castro, "Large-eddy simulation of dispersion from surface sources in arrays of obstacles," Boundary-Layer Meteorology **135**, 433–454 (2010).

[10]H. Fossum, B. P. Reif, M. Tutkun, and T. Gjesdal, "On the use of computational fluid dynamics to investigate aerosol dispersion in an industrial environment: a case study," Boundary-Layer Meteorology **144**, 21–40 (2012).

[11]Y. Liu, G. Cui, Z. Wang, and Z. Zhang, "Large eddy simulation of wind field and pollutant dispersion in downtown macao," Atmospheric environment **45**, 2849–2859 (2011).

[12]Z.-T. Xie and I. P. Castro, "Large-eddy simulation for flow and dispersion in urban streets," Atmospheric Environment **43**, 2174–2185 (2009).

[13]J. Puttock, *Stably stratified flow and dense gas dispersion* (Oxford University Press, USA, 1988).

[14]E. Wingstedt, A. Osnes, E. Åkervik, D. Eriksson, and B. P. Reif, "Large-eddy simulation of dense gas dispersion over a simplified urban area," Atmospheric Environment **152**, 605 – 616 (2017).

[15]A. Robins, P. Hayden, and E. M. M. Wingstedt, "MODITIC wind tunnel experiments," Tech. Rep. 2016/01483 (Norwegian Defence Research Establishment, 2016).

[16]T. B. Gatski and J.-P. Bonnet, *Compressibility, turbulence and high speed flow* (Academic Press, 2013).

[17]S. B. Pope, *Turbulent flows* (Cambridge University Press, 2000).

[18]M. Lesieur, O. Métais, and P. Comte, *Large-eddy simulations of turbulence* (Cambridge University Press, 2005).

[19]P. Sagaut, *Large eddy simulation for incompressible flows: an introduction* (Springer Science & Business Media, 2006).

[20]F. Stylianou, R. Pecnik, and S. Kassinos, "A general framework for computing the turbulence structure tensors," Computers & Fluids **106**, 54–66 (2015).

[21]S. C. Kassinos, W. C. Reynolds, and M. M. Rogers, "One-point turbulence structure tensors," Journal of Fluid Mechanics **428**, 213–248 (2001).

[22]S. C. Kassinos, "A structure-based model for the rapid distortion of homogeneous turbulence." (1995).

[23]A. Bhattacharya, S. C. Kassinos, and R. D. Moser, "Representing anisotropy of two-point second-order turbulence velocity correlations using structure tensors," Physics of Fluids (1994-present) **20**, 101502 (2008).

[24]C. D. Pierce and P. Moin, "Progress-variable approach for large-eddy simulation of non-premixed turbulent combustion," Journal of Fluid Mechanics **504**, 73–97 (2004).

[25]F. Ham and G. Iaccarino, "Energy conservation in collocated discretization schemes on unstructured meshes," Annual Research Briefs **2004**, 3–14 (2004).

[26]F. Ham, K. Mattsson, and G. Iaccarino, "Accurate and stable finite volume operators for unstructured flow solvers," Tech. Rep. (Center for Turbulence Research, 2006).

[27]F. Ham, "An efficient scheme for large eddy simulation of low-ma combustion in complex configurations," Annual Research Briefs, Center for Turbulence Research, Stanford University (2007).

[28]B. Cabral and L. C. Leedom, "Imaging vector fields using line integral convolution," in *Proceedings of the 20th annual conference on Computer graphics and interactive techniques* (ACM, 1993) pp. 263–270.

[29]H. Le, P. Moin, and J. Kim, "Direct numerical simulation of turbulent flow over a backward-facing step," Journal of Fluid Mechanics **330**, 349–374 (1997).

[30]J. J. Quirk, "A contribution to the great riemann solver debate," in *Upwind and High-Resolution Schemes* (Springer, 1997) pp. 550–569.

[31]G. Zhu, S. P. Arya, and W. H. Snyder, "An experimental study of the flow structure within a dense gas plume," Journal of Hazardous Materials **62**, 161–186 (1998).

[32]P. Bradshaw, "The turbulence structure of equilibrium boundary layers," Journal of Fluid Mechanics **29**, 625–645 (1967).

[33]J. S. Turner, *Buoyancy effects in fluids* (Cambridge University Press, 1979).

[34]R. L. Panton, "Overview of the self-sustaining mechanisms of wall turbulence," Progress in Aerospace Sciences **37**, 341–383 (2001).

[35]M. Vartdal, "Computing turbulence structure tensors in plane channel flow." Computers & Fluids (2016).

[36]H. E. Fossum, *Computational modeling of stably stratified, turbulent shear flows*, Ph.D. thesis, Mechanics Division, Department of Mathematics, University of Oslo (2015).